Crystal Morphology Monitoring Based on In-situ Image Analysis of L-glutamic Acid Crystallization

Zhimao Lu[a], Lin Zhang[b], Yongming Jiang[c], Chi Zhang[d], Guijuan Zhang[e], and Mengzhu Liu[f]

Faculty of Electronic Information and Electrical Engineering Dalian University of Technology, Dalian, China.

[a]zhimaolu@163.com, [b]zl221919@163.com, [c]jsasunday@163.com,[d]zhangchi6666@163.com, [e]angelinaminbing@163.com, [f]stuggle@yeah.net

Abstract. In the process of chemical industry and biological pharmacy, the morphology of the crystal plays a vital role; different morphological characteristics such as shape and size have a direct impact on production. Therefore, this paper proposes a synthetic in-situ image analysis method for monitoring the morphology of crystals based on using an invasive imaging system. The proposed method includes image preprocessing, feature extraction, morphological identification and agglomeration re-segmentation. The in-situ image is first pre-processed to eliminate the effects of water droplets, particle shadows, and uneven illumination. Then, texture features are extracted by using Improved-Basic Gray Level Aura Matrix (I-BGLAM) for different types of particles, and shape features are extracted by using image descriptors. Afterwards, the extracted features are used to morphologically identify the different particles. At last, the salient corners of the particles are detected, and a segmentation algorithm that separates individual crystals from the agglomerates is constructed by clustering the same type of salient corners. The case study and experimental results of L-glutamic acid cooling crystallization show that the image analysis method can be effectively used for morphology analysis of in-situ crystals with good precision.

Keywords: Crystal, image analysis, I-BGLAM, image descriptors, segmentation.

1. Introduction

The crystallization process has an extremely important influence on industrial production, especially in the chemical industry. The process has been widely used in solid-liquid separation, purification and crystal production in the fields of special chemical industry, biological pharmacy and agricultural chemistry [1]. With the rapid development of process analysis technology (PAT) in the chemical and biopharmaceutical fields, image analysis technology has become a new means to analyze the morphology of crystal particles [2]. The use of image analysis technology to control particle size distribution (PSD) is of great significance for accurate evaluation of the quality of final drugs and chemical products, as well as downstream processing of chemical solids [3].

Image-based methods provide the potential for both quantitative and qualitative analysis of crystals. In general, in situ crystallization process monitoring imaging systems can be broadly classified into two categories: invasive imaging systems and non-invasive imaging systems [4]. The invasive imaging system monitors the crystallization process by inserting the camera into the crystallization reaction vessel to obtain a high resolution crystal image; the non-invasive imaging system monitors the crystallization process using one or more cameras placed outside the crystallization reaction vessel [5]. The use of non-invasive imaging system can avoid the image acquisition equipment being contaminated by solution to ensure measurement accuracy, but also has the disadvantages of inconvenient fixed image acquisition equipment and low image resolution [6].

In recent years, many researchers have proposed various efficient methods of particle segmentation. J. A. Calderon De Anda proposed a multi-scale image segmentation algorithm for segmentation of crystals [7]. K. R. Periasamy proposed a multi-objective optimization (MOO) method based on

synthetic images, and combined the threshold method with the minimum error method to count the number of particles at various concentrations [8]. B. Liu proposed a top-hat transform method for improving contrast to eliminate asymmetrical illumination [9]. D. Sarkar introduced a new image segmentation method based on multivariate statistical model information, combining multivariate image analysis (MIA) with classical image analysis to extract qualitative and quantitative information of PSD [10]. R. Baratti made use of the fractal dimension (FD) in the feature analysis and energy features as input to the artificial neural network, using threshold method and wavelet algorithm to remove the image background [11]. T. E. Arnaout designed a rolling ball adaptive threshold algorithm combined with a sliding paraboloid of rotation to segment particles from the background, the algorithm is robust without using Canny edge detection and watershed algorithm [12]. B. Zhang proposed a novel image texture method based on threshold and wavelet energy analysis. The threshold method can quickly remove the background. The fractal dimension (FD) is invoked as the parameter of texture analysis for wavelet analysis, and the image texture feature is extracted by wavelet analysis [13]. J. Wan located the effective corners of the particles in the case of high concentration particles, and successfully separated the interconnected crystals by clustering of the corners and the marker-controlled watershed algorithm [14]. Y. Zhou gave specific optimization parameters for various image algorithms [15]. Y. Huo proposed a comprehensive image analysis strategy for in-situ crystal size measurement and particle segmentation, which has been shown to be effective for monitoring crystals [4]. S. Schorsch designed a new stereo image acquisition device and proposed a method based on image analysis to measure the multi-dimensional particle size distribution during crystallization [16]. Although the above advanced particle segmentation algorithm can extract some effective particles from the image, usually these algorithms take a long time, and for invasive imaging systems, problems such as water droplets and shadows cannot be solved.

Whether using invasive or non-invasive imaging systems, there are still crystal overlaps and agglomeration problems in the acquired images. The misidentification of these agglomerates into single crystals directly affects the distribution of crystal size and shape. L. M. Terdenge, A. Ferreira, S. Heisel, L. M. Terdenge, D. R. Ochsenbein used Discrimination Factorial Analysis (DFA) and Artificial Neural Networks (ANN) to divide agglomerated particles and single crystals into training sets and testing sets and conducted a variety of dataset crossover experiments, defined PI and Ag test indicators, the experiment proved that the recognition accuracy can reach 93% [17-21]. Y. Huo monitored particle agglomerations during crystallization by using microscopic double-view image analysis [22]. P. A. Larsen designed a SHARC (segmentation for high-aspect-ratio Crystals) algorithm that uses the high aspect ratio of the crystal to separate agglomerates [23]. K. Zou used the gray level co-occurrence matrix (GLCM) to extract texture features and chord-to-point distance accumulation (CPDA) algorithm for corner detection, which achieved better separation of needle-like crystals [24].

In this paper, a new image analysis method is proposed for monitoring of the morphology information of in-situ cooling crystals. The method mainly includes image preprocessing, feature extraction, morphological identification and agglomeration re-segmentation. Experimental tests of the cooling crystallization of L-glutamic acid are performed to demonstrate the effectiveness of the proposed method. For clarity, the paper is organized as follows. Experimental setup on detecting the L-glutamic acid (LGA) crystals during cooling crystallization is presented in Section 2. In Section 3, the proposed image analysis method is introduced. Section 4 shows experimental results to demonstrate the effectiveness of the proposed method. Finally, some conclusions are drawn in Section 5.

2. Experimental Setup

The crystal cooling crystallization device is illustrated in Fig 1. The main body of the crystallization reaction vessel is a 4 liter glass vessel with a sandwich for easy reaction control. The unit uses a thermostatic circulator (Product no.Julabo-CF41) and a Pt100 temperature probe. The

agitator uses a PTFE four-blade agitator with a speed range of 150-200 revolutions per minute(rpm). The invasive imaging system used in this paper consists of two high-resolution cameras developed by Hainan Six Sigma Intelligent Systems Ltd. (product no. Stereo Vision Crystal-G). The camera (UI-2280SE-C-HQ) was produced by IDS Image Development System GmbH. It used CCD sensor and USB Video Class standard to capture 6 frames per second with an image resolution of 1200*1600.

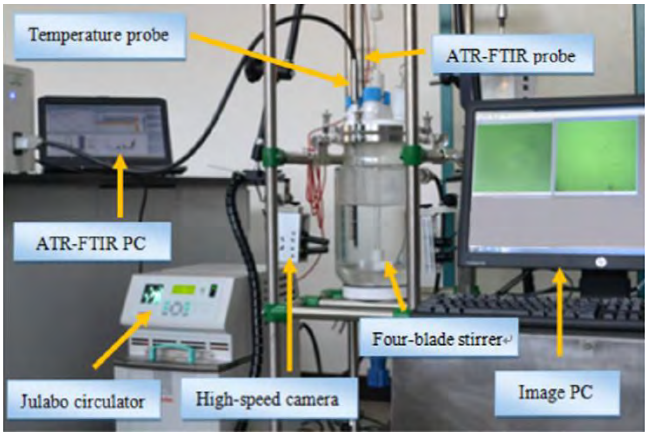

Fig. 1 Experimental set-up of the crystallizer equipped with the invasive imaging system.

In this experiment, 70 g of L-glutamic acid (chemical formula: C5H9NO4, molecular weight: 147.13 g/mol, purity: 99%) was dissolved in 2 L of fresh distilled water as the initial solution concentration, and the stirrer was rotated at a constant speed of 150 rpm. The reaction solution was first heated up to 75 ° C and held at this temperature for 90 minutes to guarantee complete dissolution of L-glutamic acid. The solution was then cooled at a cooling rate of 0.8 ° C per minute up to 15 ° C, and this temperature was maintained until the end of the experiment.

3. Image Analysis Method

Fig. 2 shows a flow chart of the method. Firstly, the image processing method is used to preprocess the acquired in-situ image to eliminate the influence of water droplets, particles shadows and uneven illumination caused by the invasive imaging system, and obtain a clean crystal image. Secondly, Improved-Basic Gray Level Aura Matrix (I-BGLAM) is used to extract texture features of the particles to judge the focusing state of the particles. The image descriptors are used to extract the shape features to distinguish the single crystals and the agglomerates for morphological identification. Finally, a segmentation algorithm is proposed to separate the agglomerates into single crystals by using the recognition and clustering of the salient corners to obtain the morphology of the crystals. The above steps will be explained in detail in the following sections.

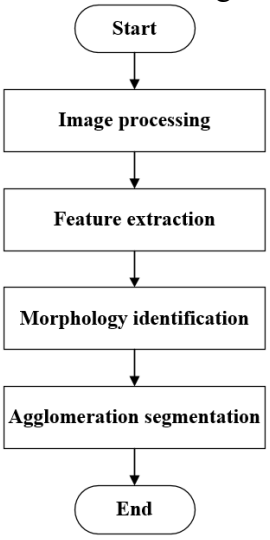

Fig. 2 Flow chart of the proposed image analysis method

3.1 Image Processing

Due to the limitations of the reaction conditions and the experimental environment, the images acquired by the invasive imaging system used in this experiment often contain a lot of noise. The more obvious and serious problems are the intrusion of the camera lens into the reaction vessel, so that the captured images contain a large number of water droplets (Fig. 3 (a)) and the particle shadows caused by uneven illumination (Fig. 3 (b)). These problems directly affect the statistics of the number of particles and the measurement of the size. In response to the above problems, an image processing method is proposed for segmenting crystal particles from a background image. Fig. 4 shows the specific process.

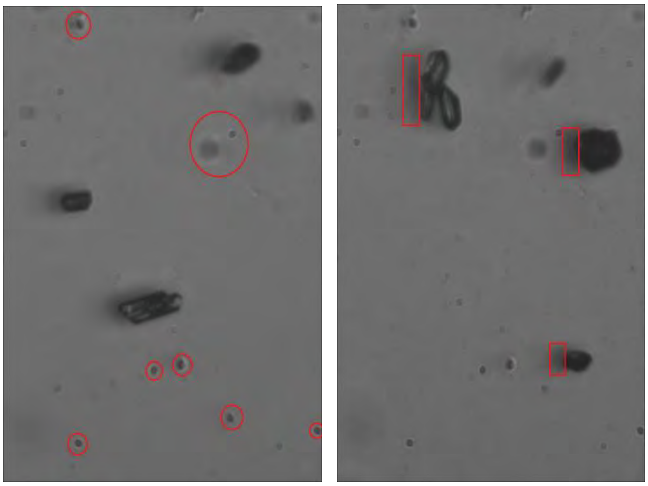

(a) (b)

Fig. 3 (a) Droplets (circled by the red circles) of particle image; (b) Particle shadow (framed by the red rectangles) of particle image

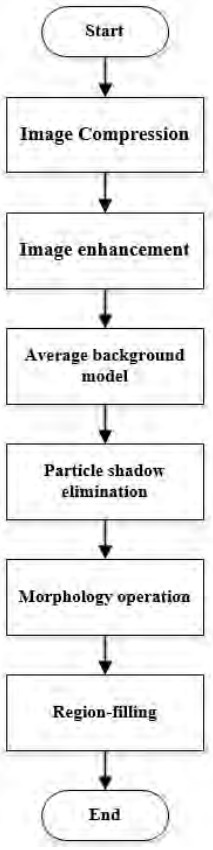

Fig. 4 Flow chart of image processing

In the course of this experiment, in order to obtain a variety of information of particles, it requires low time consumption, and large-size images will greatly reduce the processing speed and increase unnecessary processing time. Therefore, it is necessary to properly compress the image and try to

ensure that the image is reduced in size without losing valid information. The image compression algorithm based on wavelet transform has the advantages of high compression ratio and fast compression speed. On this basis, the biorthogonal wavelet function [25] is used to compress the image. The algorithm proved to have good linear phase, regularity and entire reconstruction.

In order to enhance the contrast between image background and particles and reduce the impact of uneven illumination on the experiment, this paper uses an image enhancement method to solve this problem. Retinex algorithm plays an important role in image defogging, aeronautical map, medical image and other fields, and the image enhancement effect is satisfactory. This paper uses a Multi-Scale Retinex with Color Restoration(MSRCR) algorithm [26]. The MSRCR algorithm adds a color recovery factor C to the MSR (Multi-Scale Retinex) algorithm [27] to adjust for defects in color distortion due to enhanced contrast in the local area of the image. MSRCR can be explained as:

$$R_{\mathrm{MSRCR}}(x,y) = C_i(x,y) * R_{\mathrm{MSR}}(x,y) \tag{1}$$

$$C_i(x,y) = f\left[I_i'(x,y)\right] = f\left[\frac{I_i(x,y)}{\sum_{j=1}^{N} I_j(x,y)}\right] \tag{2}$$

$$f\left[I_i'(x,y)\right] = \beta\left\{\log[\alpha I_i'(x,y)] - \log\left[\sum_{j=1}^{N} I_j(x,y)\right]\right\} \tag{3}$$

Where $R_{MSR}(x, y)$is the result of the image using the MSR algorithm, $I_i(x, y)$ represents the image of the i^{th} channel, C_i represents the color recovery factor of the i^{th} channel, and $f(\cdot)$ represents the mapping function of the color space. β is the gain constant, and α is the controlled nonlinear strength. The MSRCR algorithm uses the color recovery factor C to adjust the proportional relationship between the three color channels in the original images, thus achieving the defect of eliminating image color distortion. The results of image enhancement are shown in Fig. 5.

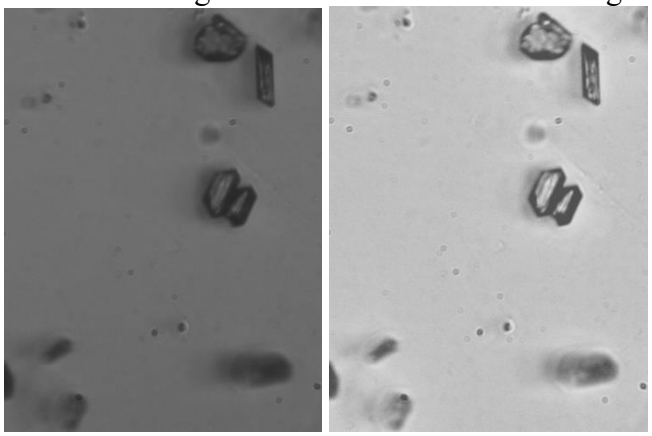

(a) (b)

Fig. 5 Image enhancement result: (a) original micrograph image; (b) enhanced image

After image enhancement, it can be observed that the particles and the background show a more distinct boundary. At the same time, the water droplets captured by the imaging system are also enhanced. Directly using the threshold methods for image segmentation will mistake the water droplets as particles, which greatly affect discrimination of crystal morphology. In order to remove the influence of water droplets, this paper proposes a particle image difference method based on average background modeling to eliminate droplets and to efficiently extract the particles from the images with complex background. First, N images to be processed are collected and their gray pixel intensity matrices are accumulated (for the crystallization experiment in this paper, a large number of experimental results show that the parameter N is 10-30 is appropriate), Then, the mean background image $f_{avg}(x, y)$ could be obtained through calculating the mean value of pixel intensity of those particle images by (4).

$$f_{\mathrm{avg}}(x,y) = \frac{1}{k}\sum_{i=1}^{k} f(x_i, y_i) \tag{4}$$

Where $f_{avg}(x, y)$ and $f(x_i, y_i)$ represent the mean image and the i_{th} image respectively; k is the number of accumulated images and x and y are the coordinates of the pixel to be processed in an $N*M$ dimensional image. Fig. 6 (a)shows the background model after constructing.

As the reaction progresses, the environmental conditions in the reactor change, and the background of the acquired image changes. It is not possible to use only a fixed background model. Therefore, it is necessary to reconstruct the background model at intervals T to adapt to the new reaction environment. In this paper, the iterative background model updating method is adopted by (5), which is to increase the background change based on the previous background model to update the background model.

$$B_n = B_{n-1} + \frac{1}{K}(f_n - f_{n-k}) \tag{5}$$

Where B_n and B_{n-1} represent the current background model and last background model respectively; f_n is the current image obtained by the imaging system; f_{n-k} is the last K_{th} image taken before current image f_n, and K represents the number of intervals designated by users. Subtraction between image f_n and image. f_{n-k} represents the increments of the particle image. Once added the increments, B_{n-1} could be updated to the new background model B_n iteratively. On the basis of obtaining the background model, this paper uses the idea of image difference, and subtracts the background model from the original image to obtain the result of removing the water droplet according to the gray pixel intensity. Fig. 6 (b) shows the result after removing the water droplets.

After the interference of the water droplets is removed, there are also significant crystal shadows in the images. If a conventional threshold method, such as direct thresholding, is used, it is difficult to find a suitable threshold to remove crystal shadows from the crystal image without affecting the crystals itself. Therefore, this paper uses a local shadow removal algorithm based on graph cut idea. Firstly, the connected area label is used to divide the crystal image into several small areas containing crystals. Secondly, the convex hull and the best-fit rectangle method are used to divide the crystals in each small region. Finally, the threshold operation is performed in each crystal region to obtain clean particles. The specific algorithm is described in [28]. Finally, the final image segmentation result is obtained using the morphological opening operation and the region filling as shown in Fig. 7.

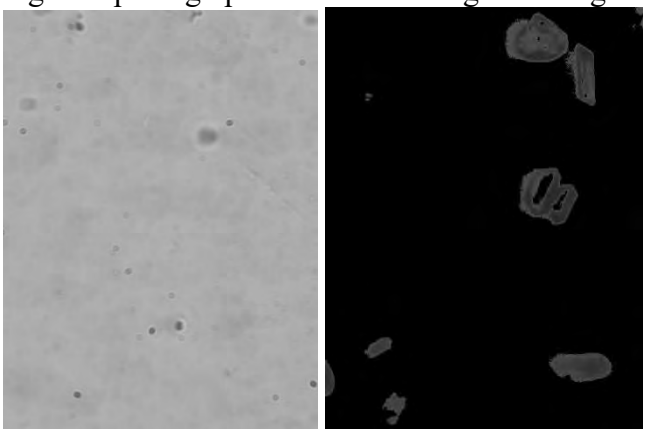

(a) (b)

Fig. 6 Image difference result: (a) mean background model; (b) the result after removing the water droplets

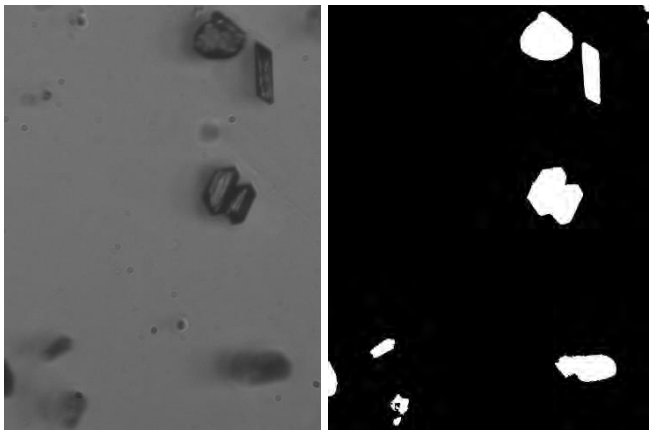

(a) (b)

Fig. 7 Image analysis results: (a) original in-situ image; (b) the result image

3.2 Feature Extraction

3.2.1 Improved-Basic Gray Level Aura Matrices:

In the process of acquiring images in the in-situ system, some particles will inevitably become out of focus due to being far away from the lens. Out-of-focus particles tend to exhibit a faint form in the image, and the surfaces look silky. While the surface texture can be clearly shown due to the sharper shooting of the particles at the focal point, so that the surfaces of the particles tend to exhibit a rough morphology. In image analysis, the gray scale is distributed in spatial position and contains a certain intensity change, at the same time, a certain repeating pattern is formed as a visual texture. The focal state of the particles can be distinguished by extracting the visual texture of the particle images. As a symbiotic probability distribution of neighborhood gray, the I-BGLAM method [29] can extract the visual texture of the image better.

In the past work, researchers mostly used Gray Level Cooccurrence Matrices (GLCM) [30-31] and Gray Level Aura Matrices (GLAM) [32-34] to extract the texture features of the image. In essence, the GLAM of an image characterizes the probability distribution of each gray level in the neighborhood of each other gray level, and thus generalizes the GLCM. In fact, when the structuring element of a neighborhood system contains only two symmetric sites, an aura matrix is a cooccurrence matrix. Although the GLAM has been successfully applied in texture modeling, the existing GLAM-based algorithms have two main problems: (1) the neighborhood system is assumed to be symmetric, (2) the number of GLAM is exponentially related to the image size. For example, even for a small image of 8*8 size, the total number of different GLAM is 2^{64}-1. Therefore, in order to solve the above problems, X. Qin proposed a new Basic Gray Level Aura Matrices(BGLAM) theory [35]. In the theoretical part, the algorithm proves that a specific set of GLAM calculated from a single-point neighborhood system can identify all the GLAM. Any GLAM can be represented as the sum of BGLAM. It is further proved that two images of the same size are the same if and only if their corresponding BGLAM is identical. In other words, the image can be uniquely represented by its BGLAM. In essence, the BGLAM of an image describes the cooccurrence probability distribution of gray levels in all possible displacement configurations.

The BGLAM is similar to the GLAM. After GLAM completes the gray level mapping, some filtering functions are needed to process the gray level values in the gray matrix to extract features, while BGLAM does not require any filters. The main advantage is the case that the features are directly calculated from the gray level mapping of the images. BGLAM is a feature extraction method for reconstructing original images from the feature values. Fig. 8 shows how to calculate an image of BGLAM. In this example, the image has a dimension of 5*5, is divided into 2 gray levels, and the dimension of the sliding window is 3*3 (that is, the nearest 8 neighbors from the center pixel). The final matrix is composed of 8 small matrices, each representing a direction with a dimension of 2*2 (since the original image is divided into 2 gray levels). First determine the direction of the number of statistics. Secondly, for each 2*2 size matrix, the number of times the pixels in the image appear in the

same position order are counted according to the position order of the pixels in the matrix $\begin{pmatrix} 00 & 01 \\ 10 & 11 \end{pmatrix}$. For example, the order from the left to the right in the horizontal direction, that is, the order in the east direction, in which the positional order is 00 occurs 6 times (orange color circled), and the positional order is 11 appears 5 times (blue color circled). The case where the positional order is 01 appears 6 times, the positional order is 10 appears 3 times. Therefore, the matrix of the eastward direction is $\begin{pmatrix} 6 & 6 \\ 3 & 5 \end{pmatrix}$. According to the same statistical method, the remaining 7 small matrices can be obtained. Once all matrices have been calculated, all the values of the matrices are concatenated to form a vector called the characteristic vector. The characteristic vector of this example is [6 3 3 4 6 6 4 4 3 8 3 2 6 6 3 5 6 3 3 4 6 4 6 4 3 3 8 2 6 3 6 5]. The length of the characteristic vector depends on the direction of the BGLAM and the size of the gray level. The formula for calculating the length of the characteristic vector is (6). Where N_f is the length of the feature vector, D is the number of directions of the BGLAM, and GL is the gray level.

$$N_f = D*GL*GL \tag{6}$$

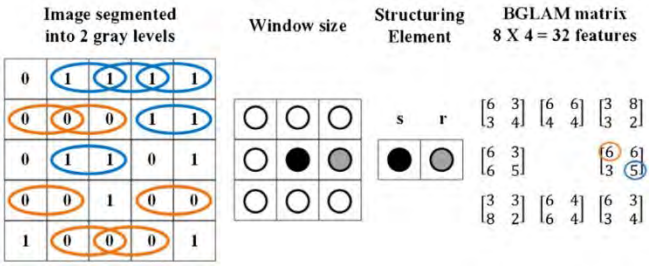

Fig. 8 BGLAM feature extraction calculation method(image from [35])

The traditional BGLAM algorithm mainly consists of two defects. One is that rotation invariance cannot be guaranteed, and the other is that there are redundant features. First, after the image is rotated, the size of the characteristic vector is similar to the original image, but the order is different. This means that the rotated image is different from the original image, which is obviously wrong. Secondly, in the above example, when the matrices of 8 directions are used, the matrix in the northwest direction is the same as the matrix in the southeast direction, and the number of times in the east direction 01 is the same as the number of times in the west direction 10, there are a large number of feature redundancy in such symmetrical directions. To solve these two defects, Zamri proposed an improved BGLAM algorithm, the I-BGLAM algorithm [29].

The I-BGLAM algorithm removes the statistical redundant direction and proposes a new way of calculating the characteristic vector, considering only the discriminant features, thus reducing the size of the feature dimension. Similarly, as shown in Fig. 8, in order to reduce the redundancy of the vector, all eight directions are no longer counted, and only the feature matrices in the north, northeast, east, and southeast directions are selected for calculation. The characteristic vector results obtained using the new calculation method are as follows:

$$[6\,6\,4\,4\,|\,3\,8\,3\,2\,|\,6\,6\,3\,5\,|\,6\,3\,3\,4] \rightarrow [\,21\;36\;15]$$
$$6+3+6+6=21,$$
$$6+4+8+3+6+3+3+3=36,$$
$$4+2+5+4=15$$

In this new way, the original 32-dimensional characteristic vector is transformed into a 3-dimensional characteristic vector with rotation invariance. Table I indicates the number of features calculated by the traditional BGLAM and the improved BGLAM algorithm. It can be observed from the table that the dimensions of the characteristic vector are greatly reduced. The length of the I-BGLAM feature vector is only related to the gray level. The calculation formula is as shown in (7), where N_f is the length of the feature vector and GL is the gray level.

$$N_f = \frac{GL*(GL+1)}{2} \tag{7}$$

Table 1 Number Of BGLAM Features For Gray Levels

Number of Gray Levels	2	4	8	16
Conventional Features (8 direction)	32	128	215	2048
Conventional Features (4 direction)	16	64	256	1024
Improved Features	3	10	36	136

3.2.2 Solidity and Concavity Index

Whether it is an invasive imaging system or a non-invasive imaging system, there are always overlapping or agglomerated particles in the images captured by the camera. Once this is the case, errors must occur in the size and shape distribution of the crystals, and the agglomerates can be mistaken as crystal growth. Only measuring the various size information of the crystal does not distinguish between single crystals and agglomerates, so it is necessary to effectively distinguish between single crystals and agglomerates. The researchers' experiments for many years prove that the image descriptors can extract the shape features of the particles well. In order to get rid of the scale interference, two dimensionless image descriptors are selected to extract the features.

- Solidity: defined as the pixel area divided by the area of the convex hull

$$I^{VEX} = \frac{A_{pro}}{A_{con}} \tag{8}$$

Where I^{VEX} represents the solidity, A_{pro} represents the projected area of the pixel, and A_{con} represents the projected area.

- Concavity Index: defined as ratio between the area of the largest concavity part of the projection and the area of the projection

$$I^{CAV} = \frac{A_{CAV_{\max}}}{A_{pro}} \tag{9}$$

Where I^{CAV} represents the concavity index, $A_{CAV_{\max}}$ represents the maximum concave area, and A_{pro} represents the projected area.

3.3 Morphology Identification

A classification problem arises when an object needs to be classified into a predefined class based on multiple observed features associated with the object. After using the feature extraction algorithm of the previous section to obtain the texture and shape features of the particles, the extracted features are used to classify the particles for morphological identification. The on-focus and out-of-focus particles are classified by texture features and the single crystals and agglomerates are classified by shape features. In this paper, the artificial neural network based on back propagation is used to identify different particles morphologically.

The artificial neural network simulates the biological nervous system. The neurons of the organism are connected by axons and dendrites. When the neurons are stimulated, the nerve impulses propagate between the neurons, and the repeated pulse stimulation makes the connections between the neurons stronger. Inspired by this, the connections (weights) between neurons in artificial neural networks are also adjusted by repeated data information "stimulation". The back propagation algorithm is used to adjust the weight. The core idea is that the training error is propagated layer by layer. The weight between each layer of neurons and the lower neurons is adjusted by the method of decreasing the error gradient.

Artificial neural networks are generally divided into three layers: input layer, hidden layer, and output layer. Both the hidden layer and the output layer have corresponding activation functions to simulate the excitation of the nerve impulses. In this paper, the back propagation neural network is used to classify the particle morphology, and the extracted features are used as the input of the neural

network, and the output is the result of the classified category. The accuracy of the final classification result depends on the proportion of the number of correctly classified samples in total sample size. The training process is divided into two parts: forward propagation and back propagation. The loss value is calculated by forward propagation, and the gradient is calculated by back propagation. The error is usually calculated by the square error loss function, and the weight value is updated according to the chain rule. In this paper, the artificial neural network is used to identify the on-focus and out-of-focus particles by using the texture features extracted by the I-BGLAM algorithm. At the same time, the features extracted by the image descriptors are used to identify single crystals and agglomerates.

3.4 Agglomeration Segmentation

After effectively distinguishing the single crystals and the agglomerates, in order to further effectively treat the agglomerates, an agglomerate segmentation algorithm based on gray analysis and edge analysis is used to divide the agglomerates into multiple single crystals [36]. The algorithm mainly consists of two parts: firstly extracting feature points from the gray image, called the salient corners; secondly, clustering the corresponding salient corners of the same type to determine the same particle.

3.4.1 Salient Corner Detection

In the present paper, a salient corner C_S is defined at a pixel $P = (x, y)$on the image spatial support D, by the location of P and the normalized vectors $\vec{u_1}$;$\vec{u_2}$ such that:

$$C_S = \left[\left(x, y, \vec{u_1}, \vec{u_2} \right)_s : (x, y) \in D, \left\| \vec{u_1} \right\|^2 = 1, \left\| \vec{u_2} \right\|^2 = 1 \right] \tag{10}$$

Where $\vec{u_1} = \frac{\overrightarrow{PP_1}}{\left\| \overrightarrow{PP_1} \right\|_2}$ and $\vec{u_2} = \frac{\overrightarrow{PP_2}}{\left\| \overrightarrow{PP_2} \right\|_2}$ are correspondent with the directions of the intersected edges (lines), $\overrightarrow{PP_1}$, $\overrightarrow{PP_2}$ at P, for any P_1 and P_2 in D.

First, all the corners are detected from the gray images by using the gray level analysis, which is called the candidate corners, and then the edge analysis is performed to find the salient corners from the candidate corners. The candidate corners is detected from the input images using the method proposed in [37], which is based on searching for the strongest point in the neighborhood (i.e., the points with the highest or lowest intensities) in a circular area of radius r. This method has stronger detection and screening capabilities than other traditional methods [38-41]. After the candidate corners are detected, the direction of the candidate corners is calculated by the directional correlation function E(θ), and the calculation formula is as shown in (11).

$$E(\theta) = \sum_{x=1}^{M} \sum_{y=1}^{N} W_C(x, y) T_\theta(x, y), \theta \in [0, 5°, ..., 360°] \tag{11}$$

where W_C is a binary edge image with a window size of $M*N$ centered at a candidate corner C, and T_θ is a line template of length L and oriented of θ°.

The directional correlation function of the salient corners has two major peaks at θ_1, θ_2, which correspond to $\vec{u_1}$ and $\vec{u_2}$ in the correlation function formula, respectively. Other corners(such as junctions) have more than two major peaks, and the correlation values at isolated points will be close to zero without significant peaks. Therefore, in the candidate corners, the correlation function has two peaks and the corners whose peak values are greater than a specific threshold are determined as the salient corners. After the salient corners are obtained, the positions and angles of these corners are further refined, and the pixel position of each corner and the two directions θ_1, θ_2 are recalculated.

3.4.2 Clustering of Salient Corners

After detecting the salient corners, this paper uses a clustering algorithm to identify particles. The algorithm determines the same particle by determining three corresponding salient corners that satisfy certain geometric conditions. First randomly select a salient corner, denoted by C_{S_A}, and then search for a set of salient corners collinear with C_{S_A}, denoted by C_{S_C}, and a group parallel to C_{S_A}, denoted by

C_{S_P}. Where the collinear salient corners C_{S_C}, contain any one of the corners on the same line and satisfy the following conditions:

$$\overrightarrow{u_{A_1}} \cdot \overrightarrow{C_{S_A} C_{S_C}} \geq \alpha \tag{12}$$

$$\overrightarrow{u_{C_1}} \cdot \overrightarrow{C_{S_A} C_{S_C}} \leq -\alpha \tag{13}$$

Where $\overrightarrow{u_{A_1}}$ and $\overrightarrow{u_{C_1}}$ are normalized vectors calculated by the formula corresponding to C_{S_A} and C_{S_C}, α is the corresponding threshold selected based on the collinear conditions. The salient corners C_{S_P} on the parallel line satisfy the following conditions:

$$\overrightarrow{u_{A_1}} \cdot \overrightarrow{u_{P_1}} \geq \alpha \tag{14}$$

Where $\overrightarrow{u_{P_1}}$ is a normalized vector corresponding to C_{S_P}. After obtaining the two groups of salient corners C_{S_C} and C_{S_P}, the two groups of corners are sorted according to the distance from C_{S_A},and two corners closest to C_{S_A} and on parallel lines with opposite direction are selected to form three salient corners together with C_{S_A} to determine a particle. The positional relationship of the three corners is as shown in Fig. 9 a single particle is determined by clustering these three salient corners, and the detailed algorithm content is referred to [42].

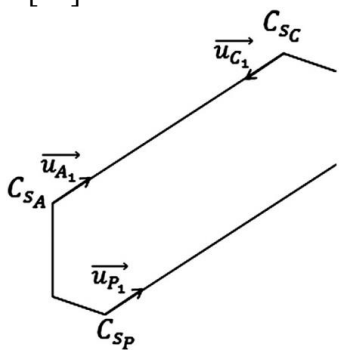

Fig. 9 Positional relationship of three salient corners (image from [36])

4. Experimental Result

4.1 Image Processing

In this paper, the image processing method is applied to test the in-situ images. After using image compression, image enhancement, mean background model, particle shadow removal, morphological operation and region filling, clean particle images are obtained in Fig. 11.

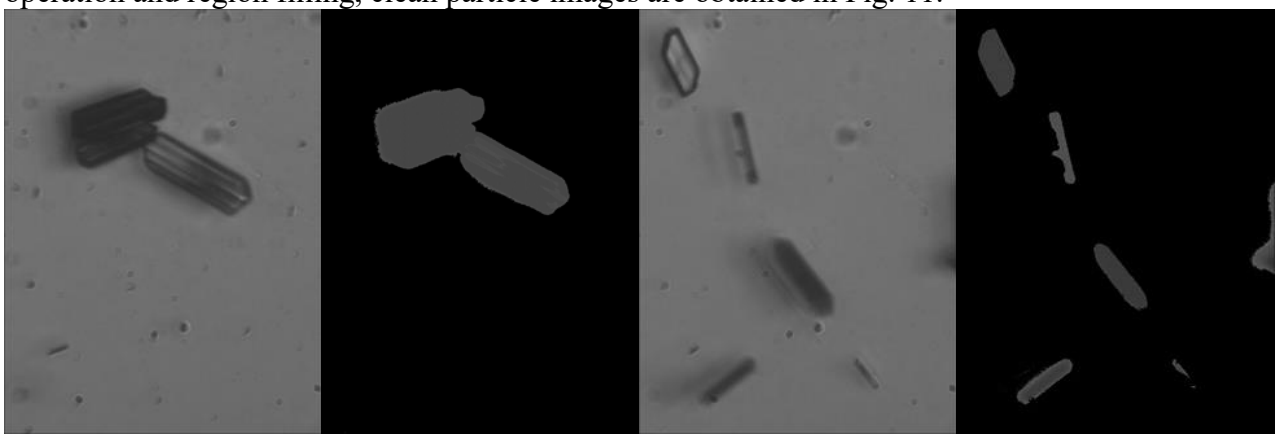

(a) (b) (c) (d)

Fig. 10 In-situ image processing results: (a), (c): original micrograph images; (b), (d): Processed images

Table 2 Comparison of Results Obtained from Nine Different Persons Manually Counting the Same 10 Image

Operator	1	2	3	4	5	6	7	8	9	average
Total	70	73	70	72	74	72	71	73	72	72
Alpha Type	39	41	40	41	39	42	39	40	41	40
Beta Type	31	32	30	31	35	30	32	33	31	32

It can be seen from the experimental results that the image processing method proposed in this paper can solve these problems well for the water droplets, uneven illumination and particle shadows existing in the in-situ image. The clean particles are obtained by this method. In order to prove the superiority of the proposed algorithm in terms of efficiency and accuracy, this paper compares the other two particle segmentation methods with the same experiment. One method is called multi-scale method [3], another method called the Synthetic Image Analysis Strategy (SIAS) [4]. First, an average of 50 images were chosen from all the images obtained from the L-glutamic acid crystallization process as experimental samples. Then nine different well-trained people were asked to segment the crystals manually and count the crystals appearing in the images. Finally, the average result of nine people was calculated as the final reference result. Table 2 shows the total number of crystals and the final average results for all 10 images of each operator.

In this paper, the three methods are used to perform particle segmentation experiments on 10 images. The results are shown in Table 3. In order to evaluate the computational efficiency of the proposed method, the timing function in Matlab is called to calculate the time of the segmentation process. All the segmentation experiments are implemented in the Matlab2018a environment, and the image size is 640*480. It can be seen from the table that the proposed method has a good segmentation rate in particle segmentation. At the same time, due to the influence of water droplets and particle shadows, it will be slightly different from the other two methods. It is worth mentioning that the method proposed in this paper only takes 1-3 seconds to process each image, and 10-30 images can complete the construction of the mean background model, while the previous method requires at least 4 seconds. The experimental results show that this method can effectively perform particle segmentation.

Table 3 Results of Segmentation by Three Methods

Segmentation Method	Proposed Method	Multi-scale Algorithm	SIAS Algorithm
Total Identified Particle Number	73	82	79
Human Operator Identified Number	70	70	70
Accuracy Rate	96%	85%	89%
Time(s)	1-3	5	4

4.2 Feature Extraction

In this paper, I-BGLAM feature extractor is used to extract the texture features of particles to distinguish between on-focus and out-of-focus particles. According to Table 1, 136 features are extracted from 16 gray levels as the texture features of the particles. The results are shown in Fig. 11. Fig. 11 (a) is the out-of-focus particle, Fig. 11 (b) is the on-focus particle, Fig. 11 (c) is the I-BGLAM characteristic figure of Fig. 11 (a), and Fig. 11(d) is the I-BGLAM characteristic figure of Fig. 11 (b). It can be seen from the figure that the I-BGLAM value of the out-of-focus particles fluctuates between 9000 and 11000, the amplitude of the fluctuation is small, the curve is relatively flat, and the I-BGLAM value of the on-focus particles fluctuates between 4000 and 18000, the amplitude of the

fluctuation is large, there are many peaks. It can be seen from the Fig. 11 (a) that the surface of the out-of-focus particles is relatively fuzzy, the spatial gray scale does not change much, and the gray scale difference of adjacent pixels is small, so the I-BGLAM curve changes little, while in the Fig. 11 (b), the surface texture of the on-focus particles is relatively clear, there are obvious texture features, and the gray scale difference between pixels is large, so many peaks are generated.

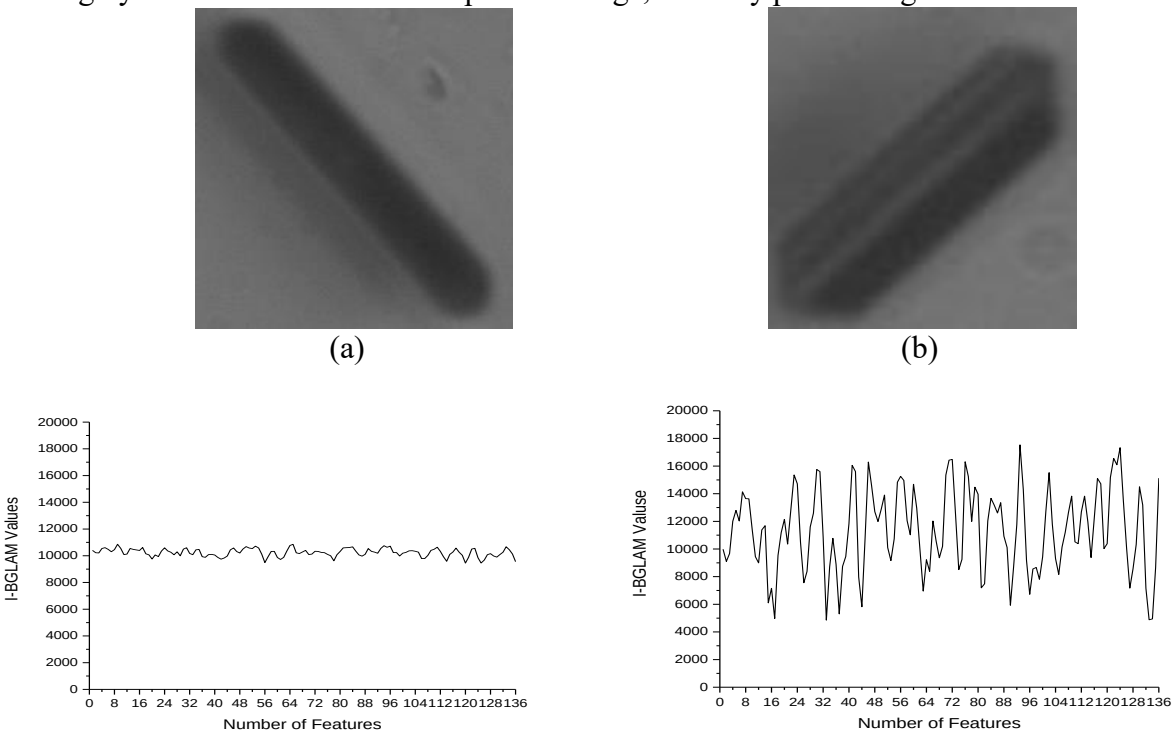

(a) (b) (c) (d)

Fig. 11 Graphs of I-BGLAM features: (a), (b): original crystal images; (b), (d): I - BGLAM characteristic figures

In this paper, two image descriptors are used to extract the shape features of particles, and the results are shown in Fig. 12. The solidity of the single crystal is close to 1, while the convexity index is close to 0. The solidity of the agglomerate is much lower than that of the single crystal, and the convexity index is much higher than that of the single crystal.

	Single Crystal	Agglomerate
Raw Image	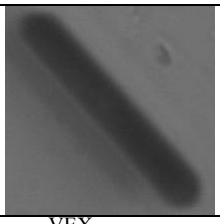	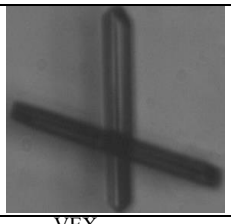
Solidity	$I^{VEX} = 0.97$	$I^{VEX} = 0.58$
Concavity Index	$I^{CAV} = 0.01$	$I^{CAV} = 0.41$

Fig. 12 The Solidity and concavity index of single crystal and agglomerate

4.3 Morphology Identification

In this paper, a total of 1000 original crystals are extracted from 300 in-situ images for morphological identification experiments. Firstly, this paper uses the back propagation based neural network to determine the focusing state of the particles. All crystal samples are divided into five groups of data sets with different proportions as different training sets and testing sets. The 136 I-BGLAM features obtained from the previous experiment are used as input of the neural network. The accuracy of the classification is calculated by ten iterations as shown in Table 4. It can be seen from Table 4 that when 80% training set and 20% testing set are used, the highest classification accuracy is 97.13%. Finally, the same experimental samples and the same method are used to extract

texture features and perform classification experiments using GLCM and GLAM methods. The experimental results are shown in Table 5. The classification accuracy rate using the GLCM method is only 62.04%, and the classification accuracy rate using the GLAM method is only 68.82%. The result is unsatisfactory, because the entropy, energy, contrast and correlation extracted by the GLCM and GLAM methods can not accurately describe the characteristics of the original image, and only extract the gray intensity of the image, and the I-BGLAM algorithm used in this paper greatly improves the accuracy of the classification, and proves the effectiveness of the algorithm in particle texture extraction.

In order to distinguish the agglomerations of crystals, two kinds of descriptors, solidity and concavity index are used to distinguish them. The solidity and concavity index are calculated for 200 single crystals and 200 agglomerates, and classified by artificial neural network. As well as prediction, using 80% training set, 20% testing set, iteration 10 times, the classification result can reach 99%.

Table 4 Classification Accuracies for 5 Sets of Data for 10 Iterations

Ratio of classification		1	2	3	4	5	6	7	8	9	10
Train:90% Test:10%	Train	97.25	97.12	96.41	97.26	97.64	98.25	98.63	97.56	98.42	97.34
	Test	92.44	92.38	95.77	94.85	93.27	93.64	94.51	94.15	93.89	92.91
Train:80% Test:20%	Train	96.56	97.26	98.46	97.11	98.15	98.14	98.22	97.64	99.38	99.10
	Test	94.21	94.25	94.62	93.12	95.66	96.29	95.43	97.13	93.27	94.52
Train:70% Test:30%	Train	97.20	97.56	98.43	98.33	98.77	98.03	98.52	97.22	97.63	95.45
	Test	95.25	94.38	96.56	96.43	95.82	94.85	94.67	95.63	96.82	96.74
Train:60% Test:40%	Train	98.43	98.67	97.29	98.69	96.53	97.56	96.94	98.13	97.85	98.28
	Test	93.26	93.96	94.54	95.68	93.76	95.24	94.38	94.94	95.26	93.46
Train:50% Test:50%	Train	97.58	98.35	98.52	97.86	98.32	98.17	97.56	96.48	95.25	98.69
	Test	92.21	93.63	93.49	94.24	95.10	94.64	94.31	94.29	94.42	94.91

Table 5 Classification Results Obtained by Different Feature Extraction Methods

Feature Extraction Method	Classification Accuracy (%)
GLCM	62.04
GLAM	68.82
I-BGLAM	97.13

4.4 Agglomeration Segmentation

The in-situ images are processed by the proposed image processing method to obtain clean particle images. The salient corners are selected by particle re-segmentation algorithm and clustered to determine individual crystals. The results of agglomeration re-segmentation are shown in Fig. 13. It can be seen from the figure that agglomerates are segmented, in which the prismatic and rectangular crystals can be well segmented, while some other irregular crystals cannot be accurately identified, the interference around them cannot be judged as a single crystal, only the main crystal can be identified.

In order to verify the effectiveness of the method, the results of expert artificial segmentation are compared with those of the method. A total of 100 crystal images are used for experiments.

The experimental results are shown in Table 6, where N_V denotes the number of crystals identified by experts and N_A denotes the number of crystals identified by particle segmentation method. N_C denotes the number of correctly identified crystals, which refers to the number of crystals simultaneously identified by the method and experts. N_M denotes the number of unrecognized crystals, which refers to the number of crystals identified by experts but not by methods. N_I denotes the number of incorrect crystals identified, that is, the number of crystals identified by the method but not by experts. The experiment is carried out at low, medium and high concentrations simultaneously. It can be seen from the table that the rate of crystal recognition decreases with the increase of overlap level, but the overall effect is very good. This result can be regarded as normal, because at high agglomeration level, the possibility of finding three corresponding salient corners belonging to the same particle will decrease, so the recognition rate will decrease.

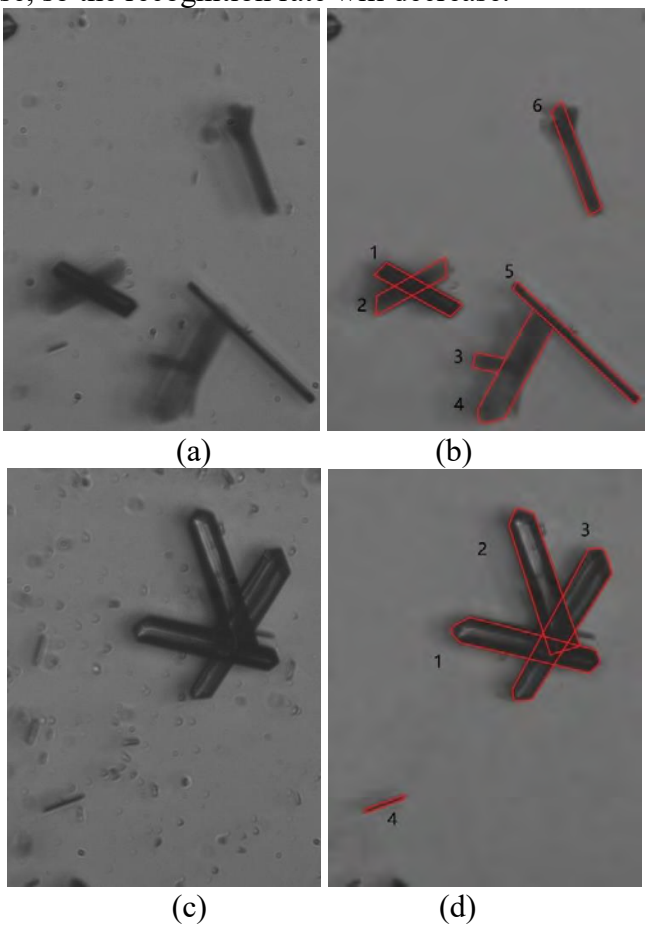

(a) (b)

(c) (d)

Fig. 13 Agglomeration re-segmentation results: (a), (c): original crystal images; (b),(d): re-segmentation results

Table 6 Quantitative Comparison of Manual Segmentation Results and Method Segmentation Results Under Different Crystal Concentrations

	Low overlap	Intermediate overlap	High overlap
N_V	72	153	308
N_A	70	142	281
N_C	68	135	253
N_M	2	11	27
N_I	2	7	28
(N_C / N_A) %	97.14	95.07	90.04
(N_M / N_V) %	2.78	7.19	8.77
(N_I / N_A) %	2.86	4.93	9.96
(N_C / N_V) %	94.44	88.24	82.14

Usually, the main reason that affects the size distribution of particles is the agglomeration, which leads to the increase of particle size, thus affecting the statistical law. Effective particle re-segmentation makes the measurement of particle size more accurate. Once the crystals are successfully segmented, the texture features of each crystal can be calculated by I-BGLAM, and then the focusing state of the crystal can be judged by the classification of artificial neural network, and then the overlapping particles can be judged. As shown in Fig. 13, Fig. 13 (b) is the result of the re-segmentation of Fig. 13 (a). crystal 1 is recognized as on-focus state, while crystal 2 is recognized as out-of-focus state. Therefore, it is judged that the two are overlapping states, and so are crystals 3, 4 and 5. Fig. 13 (d) is the re-segmentation result of Fig. 13 (c), in which crystal 1, 2 and 3 are all recognized as on-focus state, and the three are in agglomeration state. Therefore, this method can effectively distinguish overlapping particles and agglomerated particles.

The image analysis method proposed in this paper firstly extracts clean particle images from complex solution images. Secondly divide the agglomerates into multiple single crystals in the image with agglomerates, and then monitor the morphology of each crystal, including size information, texture information and so on. The previous method [28] regards agglomerates as single crystals, which in turn produces false statistical information. Taking the size information as an example, the length and width of particles obtained by the two methods are measured by the best-fit rectangle method [43], respectively, as shown in Fig. 13. It can be seen from the figure that the method of [28] regards agglomerate 1 as a crystal, which causes the increase of particle size and then produces erroneous information. The method proposed in this paper can identify agglomerates as multiple single crystals; more accurately count the size information of the crystal, and then monitor the crystal morphology.

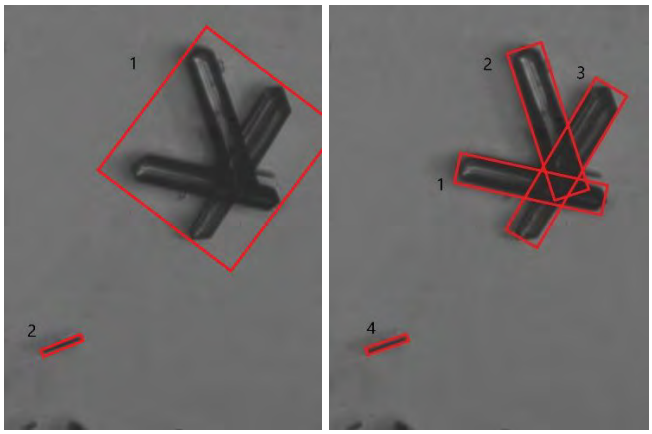

(a) (b)

	1	2
Length/μm	627.42	156.86
Width/μm	580.36	30.54
L-W ratio	1.081	5.136

(c)

	1	2	3	4
Length/μm	533.31	517.62	596.05	156.86
Width/μm	122.43	109.80	122.27	30.54
L-W ratio	4.356	4.714	4.875	5.136

(d)

Fig. 14 Statistical size results: (a), (b): image segmentation results; (c), (d): size results

5. Conclusion

An in-situ image analysis method based on invasive imaging system for crystal morphology monitoring is proposed to monitor the morphology of the crystal. The method includes image preprocessing, feature extraction, morphological identification, and agglomeration re-segmentation. The in-situ image is first pre-processed to eliminate the effects of water droplets, particle shadows, particle motion, and uneven illumination. Secondly, the effective texture features of the particles are extracted to distinguish the focusing state of the particles, and the image descriptors are used to extract the particle shape features to distinguish the single crystal from the agglomerates. Finally, a particle segmentation algorithm is used to re-segment the agglomerates and combine the texture features to identify the agglomerates. During the L-glutamic acid cooling crystallization experiment, the crystal images collected by the invasive imaging system were tested. The experimental results show that the method can be used to monitor the crystallization process, with good precision and feasibility.

Acknowledgments

Funding: This work was supported by the National Natural Science Foundation of China [grant numbers 61502124, 61473054, 91434126] and the National Thousand Talents Program of China.

References

[1]. Livk, Iztok , and V. Rehbock, "Optimal control of a batch crystallization process," J IND MANAG OPTIM, vol. 3.3, pp. 585-596, 2007.

[2]. Z. K. Nagy, G. Fevotte, H. Kramer, and L. L. Simon, "Recent advances in the monitoring, modelling and control of crystallization systems," CHEM ENG RES DES, vol. 10, pp. 1903-1922, 2013.

[3]. Y. Huo, T. Liu, H. Liu, C. Y. Ma, and X. Z. Wang, "In-situ crystal morphology identification using imaging analysis with application to the L-glutamic acid crystallization," CHEM ENG SCI, vol. 148, 2016.

[4]. Y. Huo, T. Liu, H. Liu, C. Y. Ma, and X. Z. Wang, "In-situ crystal morphology identification using imaging analysis with application to the L-glutamic acid crystallization," CHEM ENG SCI, vol. 148, 2016.

[5]. A. Borissova, et al, "In Situ Measurement of Solution Concentration during the Batch Cooling Crystallization of l-Glutamic Acid using ATR-FTIR Spectroscopy Coupled with Chemometrics," CRYST GROWTH DES, vol. 9.2, pp. 692-706, 2009.

[6]. E. Simone , A. N. Saleemi , and Z. K. Nagy, "In Situ Monitoring of Polymorphic Transformations Using a Composite Sensor Array of Raman, NIR, and ATR-UV/vis Spectroscopy, FBRM, and PVM for an Intelligent Decision Support System," ORG PROCESS RES DEV, vol. 19.1 , pp. 167-177, 2015.

[7]. J. C. D. Anda, X. Z. Wang , and K. J. Roberts, "Multi-scale segmentation image analysis for the in-process monitoring of particle shape with batch crystallisers," CHEM ENG SCI, vol. 60.4, pp. 1053-1065, 2005.

[8]. Karthik Raja. Periasamy, and L. Samavedham, "Estimation of crystal size distribution based on two dimensional characteristics: an exploration using artificial images," International Journal of Advances in Engineering Sciences & Applied Mathematics, vol. 4.1-2, pp. 78-90, 2012.

[9]. Bing-bin Liu, et al. "Automatic recognition and quantitative analysis of Ω phases in Al-Cu-Mg-Ag alloy," Journal of Central South University, vol. 21.5, pp. 1696-1704, 2014.

[10]. D. Sarkar, X. T. Doan, Z. Ying, and R. Srinivasan, "In situ particle size estimation for crystallization processes by multivariate image analysis," CHEM ENG SCI, vol. 64.1, pp. 9-19, 2009.

[11]. R. Baratti, B. Zhang, R. Willis, J. A. Romagnoli, and S .Tronci, "Image-Based Multi-Resolution-ANN Approach for On-line Particle Size Characterization," IND ENG CHEM RES, vol. 53.17, pp. 7008-70018, 2014.

[12]. T. E. Arnaout, P. J. Cullen , and C. Sullivan, "A novel backlight fiber optical probe and image algorithms for real time size-shape analysis during crystallization," CHEM ENG SCI, vol. 149, pp. 42-50, 2016.

[13]. B. Zhang, A. Abbas, and J. A. Romagnoli, "Automatic image-based estimation of texture analysis as a monitoring tool for crystal growth," CHEMOMETR INTELL LAB, vol. 121, pp. 42-51, 2013.

[14]. J. Wan, C. Y. Ma, and X. Z. Wang, "A method for analyzing on-line video images of crystallization at high-solid concentrations," Science and Technology of Particles, vol. 6, pp. 19-15, 2008.

[15]. Y. Zhou, R. Srinivasan, and S. Lakshminarayanan, "Critical evaluation of image processing approaches for real-time crystal size measurements," COMPUT CHEM ENG, vol, 33.5, pp. 1022-1035, 2009.

[16]. S. Schorsch, D. R. Ochsenbein, T. Vetter, M. Morari, and M. Mazzotti, “High accuracy online measurement of multidimensional particle size distributions during crystallization," CHEM ENG SCI, vol. 105, pp. 155-168, 2014.

[17]. L. M. Terdenge, and K. Wohlgemuth, "Impact of agglomeration on crystalline product quality within the crystallization process chain," CRYST RES TECHNOL, 2016.

[18]. A. Ferreira, N. Faria, F. Rocha, and J. A.Teixeira, "Using an Online Image Analysis Technique to Characterize Sucrose Crystal Morphology during a Crystallization Run," IND ENG CHEM RES, vol. 50.11, pp. 6990-7002.

[19]. S. Heisel, T. Kovačević, H. Briesen, G. Schembecker, and K. Wohlgemuth, "Variable selection and training set design for particle classification using a linear and a non-linear classifier," CHEM ENG SCI, vol. 173, pp. 131-144, 2017.

[20]. L. M. Terdenge, S. Heisel, G. Schembecker, and K. Wohlgemuth, "Agglomeration degree distribution as quality criterion to evaluate crystalline products," CHEM ENG SCI, vol. 133, pp. 157-169, 2015.

[21]. D. R. Ochsenbein, T. Vetter, S. Schorsch, M. Morari, and M. Mazzotti, "Agglomeration of Needle-like Crystals in Suspension: I. Measurements," CRYST GROWTH DES, vol. 15.4, pp.1923-1933, 2015.

[22]. Y. Huo, T. Liu, X. Z. Wang, C. Y. Ma, and X. Ni, "Online Detection of Particle Agglomeration during Solution Crystallization by Microscopic Double-View Image Analysis," IND ENG CHEM RES, vol. 56.39, pp. 11257-11269, 2017.

[23]. P. A. Larsen, J. B. Rawlings , and N. J. Ferrier, "An algorithm for analyzing noisy, in situ images of high-aspect-ratio crystals to monitor particle size distribution," CHEM ENG SCI, vol. 61.16, pp. 5236-5248, 2006.

[24]. K. Zou, T. Liu, Y. Huo, F. Zhang, and X. Ni, "Image analysis for in-situ detection of agglomeration for needle-like crystals," IEEE Control Conference, 2017.

[25]. R. C. Gonzalez, R. E. Woods, S. L. Eddins, DIGITAL IMAGE PROCESSING USING MATLAB. Electronic industry press, 2013.

[26]. D. J. Jobson, Z. Rahman, and G. A. Woodell, "A multiscale retinex for bridging the gap between color images and the human observation of scenes," IEEE T IMAGE PROCESS, vol. 6.7, pp. 965-976, 1997.

[27]. Z. U. Rahman, and G. A. Woodell， "Multi-scale retinex for color image enhancement," IEEE ICIP, 2002.

[28]. Z. M. Lu, F. C. Zhu, X. Y. Gao, B. C. Chen, T. Liu, and Z. G. Gao, "In-situ particle segmentation approach based on average background modeling and graph-cut for the monitoring of, l -glutamic acid crystallization," CHEMOMETR INTELL LAB, 2018.

[29]. M. I. A. P. Zamri, F. Cordova, A. S. M. Khairuddin, N. Mokhtar, and R. Yusof, "Tree species classification based on image analysis using Improved-Basic Gray Level Aura Matrix," COMPUT ELECTRON AGR, vol. 124, pp. 227-233, 2016.

[30]. Haralick, and M. R. , "Statistical and structural approaches to texture," Proceedings of the IEEE, vol. 67.5, pp. 786-804, 1979.

[31]. R. M. Haralick, K. Shanmugam , and I. Dinstein, "Textural Features for Image Classification," Studies in Media and Communication SMC-vol. 3.6, pp. 610-621, 1973.

[32]. Rosalind W. Picard, I. M. Elfadel , and A. P. Pentland, "Markov/Gibbs Texture Modeling: Aura Matrices and Temperature Effects," IEEE CVPR, 1991.

[33]. R. W. Picard, and I. M. Elfadel,"Structure of aura and co-occurrence matrices for the Gibbs texture model," Journal of Mathematical Imaging & Vision, vol. 2.1, pp. 5-25, 1992.

[34]. I. M. Elfadel, and R. W. Picard, "Gibbs Random Fields, Cooccurrences, and Texture Modeling," IEEE TPAMI, vol. 16.1, pp. 24-37, 1994.

[35]. X. Qin, and Y. H. Yang, "Basic gray level aura matrices: theory and its application to texture synthesis," Tenth IEEE International Conference on Computer Vision IEEE, 2005.

[36]. O. M. S. Ahmad, J. Debayle, N. Gherras, B. Presles, G. Fevotte, and J. C. Pinoli, "Quantification of overlapping polygonal-shaped particles based on a new segmentation method of in situ images during crystallization," Macromolecules, vol. 21.21115, pp. 12, 2012.

[37]. E. Rosten, and T. Drummond, "Fusing points and lines for high performance tracking," Computer Vision, ICCV, Tenth IEEE International Conference on, vol. 2, 2005.

[38]. S. M. Smith, and J. M. Brady,"SUSAN—A New Approach to Low Level Image Processing," IJCV, vol. 23.1, pp. 45-78, 1997.

[39]. X. Zhang, H. Wang, M. Hong, L. Xu, D. Yang, and B. C. Lovell, "Robust image corner detection based on scale evolution difference of planar curves," Pattern Recognition Letters, vol.30.4, pp. 449-455, 2009

[40]. F. Shen, and H. Wang, "Corner detection based on modified Hough transform," Pattern Recognition Letters, vol. 23.8, pp. 1039-1049, 2002.

[41]. C. H. Teh, and R. T. Chin, "On the detection of dominant points on digital curve," IEEE TPAMI, vol. 11.8, pp. 859-872, 1989.

[42]. O. S. Ahmad, J. Debayle, and J. C. Pinoli, "A geometric-based method for recognizing overlapping polygonal-shaped and semi-transparent particles in gray tone images," Pattern Recognition Letters, vol. 32.15, pp. 2068-2079, 2011.

[43]. W. Wang, "Image analysis of particles by modified Ferret method: best-fit rectangle," Powder Technology, vol.165.1, pp. 1-10, 2006.